ETH zürich

ETH Library

The metastatic spread of breast cancer accelerates during sleep

Journal Article

Author(s):
Diamantopoulou, Zoi; Castro-Giner, Francesc; Schwab, Fabienne Dominique; Foerster, Christiane; Saini, Massimo; Budinjas, Selina; Strittmatter, Karin; Krol, Ilona; Seifert, Bettina; Heinzelmann-Schwarz, Viola; Kurzeder, Christian; Rochlitz, Christoph; Vetter, Marcus; Weber, Walter Paul; Aceto, Nicola

Publication date:
2022-07-07

Permanent link:
https://doi.org/10.3929/ethz-b-000555910

Rights / license:
In Copyright - Non-Commercial Use Permitted

Originally published in:
Nature 607(7917), https://doi.org/10.1038/s41586-022-04875-y

Funding acknowledgement:
101001652 - Tumor-lock: forbid the generation of circulating tumor cells (EC)
801159-21 - Breast cancer metastasis TO the Bone with a first-of-its-kind 3D device that recapitulates physiological tissue-level complexity. (EC)
190077 - SNF-Förderungsprofessur PP00P3_190077 (SNF)

This page was generated automatically upon download from the ETH Zurich Research Collection.
For more information, please consult the Terms of use.

The metastatic spread of breast cancer accelerates during sleep

Zoi Diamantopoulou[1], Francesc Castro-Giner[1], Fabienne Dominique Schwab[2,3], Christiane Foerster[4,5], Massimo Saini[1], Selina Budinjas[1], Karin Strittmatter[1], Ilona Krol[1], Bettina Seifert[6], Viola Heinzelmann-Schwarz[3], Christian Kurzeder[3,4], Christoph Rochlitz[7], Marcus Vetter[6], Walter Paul Weber[4,5], & Nicola Aceto[1,*].

[1] Department of Biology, Institute of Molecular Health Sciences, Swiss Federal Institute of Technology (ETH) Zurich, 8093 Zurich, Switzerland
[2] Department of Biomedicine, University of Basel, 4058 Basel, Switzerland
[3] Department of Gynecologic Oncology, University Hospital Basel, 4031 Basel, Switzerland
[4] Breast Care Center, University Hospital Basel, 4031 Basel, Switzerland
[5] Department of Breast, Abdomen and Pelvis, University Hospital Basel and University of Basel, 4031 Basel, Switzerland
[6] Department of Hematology and Oncology, Cantonal Hospital Basel-Land, 4410 Liestal, Switzerland
[7] Department of Medical Oncology, University Hospital Basel, 4031 Basel, Switzerland

*Correspondence:
Prof. Nicola Aceto
Swiss Federal Institute of Technology (ETH) Zurich
nicola.aceto@biol.ethz.ch

Abstract

The metastatic spread of cancer is achieved by the hematogenous dissemination of circulating tumor cells (CTCs). Generally, however, the temporal dynamics that dictate the generation of metastasis-competent CTCs are largely uncharacterized, often assuming that CTCs are constantly shed from growing tumors or shed as a consequence of mechanical insults[1]. Here, we observe a striking and unexpected pattern of CTC generation dynamics in both patients with breast cancer and mouse models, highlighting that the vast majority of spontaneous CTC intravasation events occur during the rest phase. Further, we demonstrate that rest-phase CTCs are highly metastasis-prone, while CTCs generated during active phase are devoid of metastatic ability. Mechanistically, single cell-resolution RNA sequencing analysis of CTCs reveals a dramatic upregulation of mitotic genes exclusively during the rest phase in both patients and mouse models, enabling metastasis proficiency. Systemically, we find that key circadian rhythm hormones such as melatonin, testosterone and glucocorticoids dictate CTC generation dynamics, and as a consequence, that insulin directly promotes tumor cell proliferation *in vivo*, yet in a time-dependent manner. Thus, the spontaneous generation of CTCs with a high proclivity to metastasize does not occur continuously but it is concentrated within the rest phase of the host, providing a new rationale for time-controlled interrogation and treatment of metastasis-prone cancers.

89
90
91 **Main**
92
93 Circulating tumor cells (CTCs) are pioneers of the metastatic cascade in several cancer types,
94 including breast cancer[1]. The factors that regulate spontaneous CTC intravasation in
95 physiological settings are poorly understood, and the general assumption is that CTCs are
96 constantly generated from invasive cancerous tissues[2], or generated upon mechanical cues such
97 as surgery[3] or physical activity[4]. In patients and in mouse cancer models, the exact timing of
98 the events that characterize metastatic cancer progression, as well as the principles that dictate
99 CTC intravasation and their proclivity to metastasize are unclear. A better understanding of
100 these processes may result in new approaches for cancer investigation and treatment.
101
102
103 **Circadian rhythm and CTC intravasation**
104
105 We first sought to determine CTC abundance and composition in hospitalized women with
106 progressive breast cancer that had no treatment or were temporarily off-treatment and that
107 consented to donate blood during the active (10:00am) and rest (4:00am) phase of the same
108 day, including a total of 30 patients (**Fig. 1a**). Of these, 21 patients were diagnosed with early
109 breast cancer (no metastasis) and 9 were diagnosed with stage IV metastatic disease at the time
110 of blood sampling (**Supplementary Table 1**). Strikingly, upon antigen-agnostic microfluidic
111 capture of CTCs and confirmation via immunofluorescence staining[5], we found the vast
112 majority of CTCs (78.3%) in samples obtained at nighttime during rest phase, including single
113 CTCs, CTC clusters and CTC-white blood cell (WBC) clusters (**Fig 1a**, **Extended Data Fig.**
114 **1a** and **Supplementary Table 1**). To test the generality of these findings and to finely
115 characterize the precise timing of the events, we made use of four different breast cancer mouse
116 models, including human breast CTC-derived xenografts (NSG-CDX-BR16), xenografts with
117 established human breast cancer cells (NSG-LM2) or mouse breast cancer cells (NSG-4T1), as
118 well as an immune-competent syngeneic breast cancer model (BALB/c-4T1). Upon
119 transplantation of breast cancer cells in the mammary fat pad and tumor growth, we examined
120 spontaneous CTC generation over time by means of terminal blood sampling and microfluidic
121 CTC capture. Consistently with patient data, we found the vast majority of CTC events (99.2%
122 in NSG-LM2, 97% in NSG-CDX-BR16, 93.8% in NSG-4T1, 87% in BALB/c-4T1) to be
123 present in samples obtained via cardiac puncture during the mouse rest phase (corresponding
124 to daylight time, given the inverted circadian rhythm of rodents compared to humans[6]) (**Fig.**
125 **1b,c** and **Extended Data Fig. 1a**). More precisely, when performing a time-kinetic analysis of
126 a 24-hour time period at intervals of 4 hours, we observed a very prominent oscillatory pattern
127 of CTC release, peaking between 4-12 hours *Zeitgeber* time (ZT; with ZT0 defined as 06:00
128 am when the lights turn on, whereas ZT12 as 06:00 pm when the lights turn off) corresponding
129 to their rest phase (**Fig. 1b** and **Extended Data Fig. 1b**) in mice with analogous tumor burden
130 (**Extended Data Fig. 1c,d**). When focusing on the two most representative timepoints for rest
131 (ZT4) and active (ZT16) phase of the mouse circadian rhythm, we observe dramatic differences
132 in absolute and normalized CTC counts in all tested models, with a 6-to-88-fold increase for

single CTCs, 12-to-278-fold increase for CTC clusters and 8-to-34 fold-increase for CTC-WBC clusters during ZT4 (**Fig. 1c** and **Extended Data Fig. 1e-g**), while no changes are observed in the ratio of various CTC types (**Extended Data Fig. 1h**). Further, we identified highly similar (yet, even more pronounced) oscillatory patterns in CTC abundance when blood samples were obtained directly from the tumor draining vessel (**Fig. 1b** and **Extended Data Fig. 2a-e**). Given these results, the extremely short circulation half-life of CTCs[7,8], and their similar clearance rate during different timepoints of the rest and active phase (**Extended Data Fig. 2f,g**), we conclude that the major differences in CTC abundance observed during the rest *versus* active phase are to be ascribed to differences in intravasation rates. We then attempted to perturb the physiological rhythm of tumor-bearing mice by different means. Firstly, on the one side, we used well-established methods to shift the regular light-dark (LD) cycle, provoking a jet-lag effect[9], and on the other side we treated control and jet-lagged mice with melatonin, a key hormone that regulates the sleep cycle (**Extended Data Fig. 3a**). Strikingly, when analyzing blood in all mice at ZT4, we find that jet lag induction leads to a 38-to-282-fold decrease for single CTCs, 63-to-484-fold decrease for CTC clusters and 28-to-219-fold decrease for CTC-WBC clusters compared to control mice and with no changes in primary tumor size (**Extended Data Fig. 3b-d**). Further, when treating tumor-bearing mice with melatonin (daily, 2h before the start of the rest phase), and exposing them to a jet-lagged or regular light-dark cycle for a total duration of 22 days, we find a remarkable melatonin-induced increase in single CTCs, CTC clusters and CTC-WBC clusters production in all cases, rescued by the melatonin receptor antagonist luzindole (**Extended Data Fig. 3e**). Along with the effects of melatonin in increasing CTC production and luzindole in decreasing it without affecting primary tumor size, we observe an augmented or reduced metastatic burden, respectively (**Extended Data Fig. 3f,g**). We then exposed tumor-bearing mice to altered LD cycles. We used a long-day photoperiod (14:10 LD), as well as two different T-cycles with LD cycles that differ from 24-hrs (20-t 10:10 LD and 28-t 14:14 LD, respectively) and tested their effect on CTC generation. We observe a consistent increase in CTC counts during the rest phase in each of these light conditions (**Extended Data Fig. 4a-d**), suggesting a key role for light exposure, and its consequences, to CTC intravasation. Lastly, given the oscillatory pattern of CTC intravasation and its relation to the circadian rhythm, we tested whether this pattern was abolished in the context of a syngeneic transplantation of E0771.lmb mouse cancer cells in either wild type BL/6 mice (BL/6-E0771.lmb) or in *Bmal1* homozygous knockout mice (BL/6-*Bmal1*$^{-/-}$-E0771.lmb), the only arrhythmic single gene knockout model[10] (**Fig. 1d**). We find that, while CTC counts from both cardiac puncture and the TDV follow a typical oscillatory pattern in control BL/6-E0771.lmb mice, oscillation in CTC counts is lost in BL/6-*Bmal1*$^{-/-}$-E0771.lmb mice (**Fig. 1d** and **Extended Data Fig. 4e**). Of note, BL/6-*Bmal1*$^{-/-}$-E0771.lmb mice generally fail to generate CTCs despite identical tumor size and timing of sample collection compared to BL/6-E0771.lmb control mice (**Extended Data Fig. 4f,g**), highlighting that a disruption of the master regulator of the circadian clock results in abolished CTC intravasation. Taken together, these results demonstrate that CTCs are not shed continuously during tumor progression, but the greatest release of single and clustered CTCs is achieved during the rest phase in both patients with breast cancer and mouse models.

177
178 **Time-dependent metastasis-forming activity of CTCs**
179
180 We next investigated whether, additionally to the increased production during rest phase, CTCs
181 that are generated during different phases of the circadian rhythm also harbor a different
182 potential to successfully metastasize. To this end, we used the NSG-LM2 xenograft model,
183 exclusively labelled with either GFP or RFP, and upon tumor development, we isolated
184 spontaneously-shed CTCs at ZT4 (GFP-labelled) or ZT16 (RFP-labelled) by microfluidics-
185 based capture. With a robotic micromanipulator, we isolated 150 ZT4-generated GFP-labelled
186 CTCs and 150 ZT16-generated RFP-labelled CTCs, simultaneously, each of which composed
187 of 110 single CTCs, 35 CTC clusters and 5 CTC-WBC clusters (representing typical CTC
188 ratios in the NSG-LM2 model), and co-injected them through the tail vein of tumor-free
189 recipient mice at different timepoints of the circadian rhythm (ZT0, ZT4, ZT12, ZT16) to
190 measure their direct metastatic ability (**Fig. 2a**). Through *in vivo* bioluminescence imaging, we
191 find the highest metastatic burden during the rest phase, and in particular at ZT4 (**Fig. 2b**). To
192 dissect whether these metastases were derived from ZT4 or ZT16 CTCs, we conducted
193 immunohistochemical analysis of the lungs with anti-GFP and anti-RFP antibodies.
194 Remarkably, we find that the vast majority of metastases derives from ZT4-generated GFP-
195 labelled CTCs (**Fig. 2c**). These results highlight a substantial contribution of ZT4 CTCs to
196 metastasis formation, as well as a higher proclivity of ZT4 CTCs to form metastasis when
197 injected in mice during their rest phase. Next, we sought to extend our findings to additional
198 models and to precisely quantitate the metastatic ability of rest phase *versus* active phase single
199 CTCs, CTC clusters and CTC-WBC clusters, individually. We made use of both the NSG-
200 CDX-BR16 and NSG-LM2 xenograft models and upon tumor development, we isolated
201 spontaneously-shed CTCs by microfluidics-based capture. With a robotic micromanipulator,
202 we then isolated 100 single CTCs, 100 CTCs from CTC clusters and 100 CTCs from CTC-
203 WBC clusters of mice during their rest (ZT4) or active (ZT16) phase, respectively, and injected
204 them through the tail vein of tumor-free recipient mice at ZT12 to measure their direct
205 metastatic ability (**Fig. 2d**). By means of bioluminescence imaging, we confirm that CTCs
206 obtained during ZT4 exhibit an extraordinary metastasis-forming capacity compared to CTCs
207 that are obtained during ZT16 (**Fig. 2e** and **Extended Data Fig. 5a-f**). Of note, when isolated
208 during the rest phase and compared to the active phase, CTC clusters and CTC-WBC clusters
209 appear to be more significantly endowed with metastasis-forming properties compared to
210 single CTCs (**Fig. 2e** and **Extended Data Fig. 5a-f**), suggesting that most of the rest phase-
211 dependent metastatic spread of breast cancer could be ascribed to both homotypic and
212 heterotypic CTC clusters. Together, these results suggest that not only are CTC intravasation
213 rates increased, but also that their metastatic ability is augmented during the rest phase.
214
215
216 **Expression profile of CTCs during the rest and active phase**
217
218 Next, we sought to investigate molecular features determining the differential ability of CTCs
219 to seed metastasis during rest and active phase, respectively. Upon mammary fat pad
220 engraftment of BR16 and LM2 breast cancer cells, tumor growth and spontaneous CTC

221 generation, we isolated single CTCs, CTC clusters and CTC-WBC clusters during rest (ZT4)
222 and active (ZT16) phase of the mouse circadian rhythm, and subjected them individually to
223 single cell-resolution RNA sequencing[11,12] (**Fig. 3a**). In total, upon filtering for high-quality
224 samples (i.e. taking into account the number of expressed genes per cell, the total number of
225 reads per cell and the proportion of reads aligning to mitochondrial genes; see methods
226 section), we obtained a total of 138 CTCs from the NSG-CDX-BR16 model and 108 CTCs
227 from the NSG-LM2 model, representing all types of CTCs at ZT4 and ZT16. Using principal
228 components analysis, we find that time point (ZT4 *versus* ZT16) is a key feature driving
229 variance of CTC gene expression (**Fig. 3b** and **Extended Data Fig. 6a**), suggesting time point-
230 driven gene expression changes. Differential gene expression of samples isolated during the
231 rest (ZT4) *versus* the active (ZT16) phase reveals a set of 121 upregulated genes in ZT4 CTCs
232 (log2 fold-change ≥ 0.5 and false discovery rate (FDR) ≤ 0.05) and a set of 156 upregulated
233 genes in ZT16 CTCs (log2 fold-change ≤ -0.5 and false discovery rate (FDR) ≤ 0.05) (**Fig. 3c**
234 and **Supplementary Table 2**). Of note, we observe that the majority of the genes defining ZT4
235 and ZT16 expression signatures are consistently found highly upregulated (i.e. fold change) in
236 all types of CTCs, yet statistical significance is highest in CTC clusters and CTC-WBC clusters
237 (**Extended Data Fig. 6b,c**). This is consistent with a higher variability and higher dropout rate
238 expected in single cell samples. Gene set enrichment analysis of genes upregulated during ZT4
239 and ZT16 highlights a highly consistent activity of pathways that support mitosis and cell
240 division during ZT4 (adjusted P value ≤ 0.0001), mirrored by pathways that support ribosomal
241 biogenesis and translation of genes during ZT16 (adjusted P value ≤ 0.0001) (**Fig. 3d,e** and
242 **Extended Data Fig. 6d,e** and **Supplementary Table 3**). These findings are consistent with
243 prototypical gene expression timing in eukaryotic cells, i.e. comprising recurring ribosome
244 biogenesis and gene translation phases followed by the expression of cell cycle progression
245 genes and the execution of cellular division within a 24h time frame[13]. Of note, in human CTCs
246 isolated from breast cancer patients during the active (10:00 am) and rest (4:00 am) phase of
247 the same day, we confirm the same pattern of gene expression and pathway activity as observed
248 in mouse models (**Fig. 3f** and **Extended Data Fig. 6e**). Gene expression changes ascribed to
249 cell division and translation and inferred at timepoints ZT4 and ZT16, respectively, are also
250 consistently observed across different time points during the rest and active phase (**Fig. 3g** and
251 **Extended Data Fig. 6f**). Given the short half-life of CTCs, we reasoned that oscillatory
252 changes in cellular proliferation could also be visible at the level of the primary tumor when
253 analyzed at different times. Accordingly, when staining for the proliferation marker Ki67 in
254 tumors from the NSG-CDX-BR16 and the NSG-LM2 models, along with their CTCs, we find
255 a remarkable upregulation of Ki67 during the rest phase (**Fig. 3h** and **Extended Data Fig. 7**)
256 and consistent with the timing of highest CTC intravasation and expression of mitosis-related
257 genes. Together, molecular gene expression analysis of CTCs from patients and mouse models,
258 isolated during the rest and active phase, highlights very distinct gene expression patterns.
259 During the rest phase, gene expression is dominated by cell division and mitosis genes while
260 during the active phase we observe high ribosome biogenesis activity. This oscillatory
261 proliferation timing is not only observed in CTCs but also in the primary tumor, suggesting
262 this as a general phenomenon occurring to breast cancer cells during disease progression.
263

264
265 **Regulators of CTC intravasation**
266
267 Mechanistically, to identify the master regulators of circadian rhythm-driven CTC generation
268 and proliferation, we took several approaches. We first asked whether the expression of
269 prototypical circadian clock genes in cancer cells changed between the rest (ZT4) and active
270 (ZT16) phase. Similarly to previous reports highlighting disruption of rhythmicity in circadian
271 clock genes expression in cancer[14,15], we could not detect differential expression in CTCs or
272 primary tumor cells (**Extended Data Fig. 8a-c**), while we could confirm rhythmicity in non-
273 neoplastic tissues (**Extended Data Fig. 8c**). We next asked whether oscillations in CTC counts
274 could be explained by changes in interstitial fluid pressure, differential interplay with immune
275 cells and damages due to different hemolysis rates during different phases of the circadian
276 rhythm. Notably, we found no difference in YAP and TAZ expression levels or localization
277 (as sensors of interstitial pressure), in the abundance of circulating or tumor-infiltrated immune
278 cells, nor in apoptotic levels of CTCs during the rest (ZT4) *versus* active (ZT16) phase
279 (**Extended Data Fig. 9a-f**). Lastly, we interrogated our RNA sequencing data from CTCs of
280 xenografts and patients to determine the expression levels of receptors for well-known
281 circadian rhythm-regulated hormones, growth factors or molecules, reasoning that the daily
282 oscillation of their systemic levels could affect cancer cells in a time-dependent fashion. We
283 evaluated the expression of 63 receptors for circadian rhythm-regulated candidates
284 (**Supplementary Table 4**), looking for those with high expression in the vast majority of CTCs
285 and independently of a specific timepoint (i.e. stable expression over time and activity
286 proportional to the levels of their ligand). With these criteria, we find that expression of the
287 glucocorticoid receptor, androgen receptor and insulin receptor is highly represented among
288 single CTCs, CTC clusters and CTC-WBC clusters (**Extended Data Fig. 10a**), suggesting the
289 involvement of their ligands in timepoint-driven CTC generation and proliferation (**Fig. 4a**).
290 To test this hypothesis, we first treated tumor-bearing mice with either dexamethasone (specific
291 glucocorticoid receptor ligand) or testosterone (the main androgen receptor ligand),
292 respectively, both of them found at high levels in physiological conditions at the onset of the
293 active phase[16,17], i.e. when CTC numbers are low. Accordingly, both a single treatment with
294 dexamethasone at 4 mg/kg during the rest phase (ZT2) and implantation of a testosterone pellet
295 (slow, continuous release) resulted in a remarkable reduction in single CTC, CTC clusters and
296 CTC-WBC clusters when sampled at peak time during the rest phase (ZT4) (**Fig. 4b,c and**
297 **Extended Data Fig. 10b-f**). Of note, while treatment with dexamethasone or testosterone did
298 not affect primary tumor size (**Extended Data Fig. 10c,d**), we observed a reduction in the
299 metastatic burden of testosterone-treated mice (**Extended Data Fig. 10e**), consistent with a
300 prolonged suppression of CTCs generation alongside the continuous testosterone release from
301 the pellet. Further, given the well-established link between insulin stimulation and subsequent
302 cell growth and division[13,18], we asked whether insulin oscillations (with insulin being higher
303 during the active phase upon glucose intake in physiological conditions[19]) could also influence
304 breast cancer cell proliferation timing and intravasation, i.e. whether insulin stimulation during
305 the rest phase could invert the dynamics of CTC release and proliferation. To address this, upon
306 tumor development, we treated tumor-bearing mice daily (during the rest phase, at ZT3) for
307 one week with 0.7 U/kg of insulin and 1g/kg glucose, and quantified CTC abundance during

308 the rest and active phase, respectively. Consistently, we find that insulin treatment during the
309 rest phase decreases CTC intravasation at ZT4, and increases it at ZT16 (**Fig. 4d**) with no
310 significant changes in primary tumor volume (**Extended Data Fig. 10g**,**h**). Of note, treatment
311 with insulin during the rest phase also inverts the proliferation cycle of breast cancer cells, i.e.
312 it decreases proliferation during the rest phase and it increases it during the active phase
313 (**Fig.4e**). Together, we find that proliferation and intravasation of breast cancer cells are
314 dictated by daily oscillations in key circadian rhythm-regulated hormones, whose action
315 influences breast cancer metastasis dynamics.
316
317
318 **Discussion**
319
320 Our data provide new insights into the processes that dictate the generation of metastasis-
321 competent CTCs. Previous reports have suggested a role of the circadian rhythm in
322 tumorigenesis, mostly involving epidemiological studies and linking circadian rhythm
323 disruption to accelerated onset of cancer[15,20,21]. Yet, dynamics that prospectively govern
324 metastatic disease progression in this context remained poorly characterized. More recent
325 studies using *in vivo* imaging technologies and interrogation of physiological models have
326 highlighted various mechanisms adopted by cancer cells during the intravasation process[22,23,24],
327 however, a detailed understanding of the specific timing of CTC intravasation has been lacking.
328 We find that, in both patients with breast cancer and mouse models, generation of CTCs is
329 highly restricted to the rest phase, and that rest-phase CTCs are endowed with a much greater
330 metastatic proclivity compared to active-phase CTCs. This augmented metastatic ability is
331 conferred by high proliferation rates that occur in a time-dependent manner and it is influenced
332 by the action of circadian rhythm-regulated hormones, suggesting the need for time-controlled
333 approaches for the characterization and treatment of breast cancer. These could include the
334 interrogation of clinical samples at highly controlled timepoints to minimize variability, as well
335 as cancer treatment approaches that are tuned to be maximally effective during the rest phase.
336
337
338
339 **References**
340
341 1. Pantel, K. & Speicher, M. R. The biology of circulating tumor cells. *Oncogene* **35**, 1216–
342 1224 (2016).
343 2. Alix-Panabières, C. & Pantel, K. Circulating tumor cells: liquid biopsy of cancer. *Clin.*
344 *Chem.* **59**, 110–118 (2013).
345 3. Li, S. *et al.* Less micrometastatic risk related to circulating tumor cells after endoscopic
346 breast cancer surgery compared to open surgery. *BMC Cancer* **19**, 1070 (2019).
347 4. Zhu, X. *et al.* In vivo flow cytometry reveals a circadian rhythm of circulating tumor cells.
348 *Light Sci. Appl.* **10**, 110 (2021).
349 5. Szczerba, B. M. *et al.* Neutrophils escort circulating tumour cells to enable cell cycle
350 progression. *Nature* **566**, 553–557 (2019).

351 6. Ripperger, J. A., Jud, C. & Albrecht, U. The daily rhythm of mice. *FEBS Lett.* **585**, 1384–
352 1392 (2011).
353 7. Aceto, N. *et al.* Circulating tumor cell clusters are oligoclonal precursors of breast cancer
354 metastasis. *Cell* **158**, 1110–1122 (2014).
355 8. Sasportas, L. S. & Gambhir, S. S. Imaging circulating tumor cells in freely moving awake
356 small animals using a miniaturized intravital microscope. *PloS One* **9**, e86759 (2014).
357 9. Papagiannakopoulos, T. *et al.* Circadian Rhythm Disruption Promotes Lung
358 Tumorigenesis. *Cell Metab.* **24**, 324–331 (2016).
359 10. Bunger, M. K. *et al.* Mop3 is an essential component of the master circadian pacemaker in
360 mammals. *Cell* **103**, 1009–1017 (2000).
361 11. Macaulay, I. C. *et al.* Separation and parallel sequencing of the genomes and
362 transcriptomes of single cells using G&T-seq. *Nat. Protoc.* **11**, 2081–2103 (2016).
363 12. Picelli, S. *et al.* Full-length RNA-seq from single cells using Smart-seq2. *Nat. Protoc.* **9**,
364 171–181 (2014).
365 13. Polymenis, M. & Aramayo, R. Translate to divide: control of the cell cycle by protein
366 synthesis. *Microb. Cell Graz Austria* **2**, 94–104 (2015).
367 14. Masri, S. & Sassone-Corsi, P. The emerging link between cancer, metabolism, and
368 circadian rhythms. *Nat. Med.* **24**, 1795–1803 (2018).
369 15. Kettner, N. M., Katchy, C. A. & Fu, L. Circadian gene variants in cancer. *Ann. Med.* **46**,
370 208–220 (2014).
371 16. Ikeda, Y., Kumagai, H., Skach, A., Sato, M. & Yanagisawa, M. Modulation of circadian
372 glucocorticoid oscillation via adrenal opioid-CXCR7 signaling alters emotional behavior.
373 *Cell* **155**, 1323–1336 (2013).
374 17. Lucas, L. A. & Eleftheriou, B. E. Circadian variation in concentrations of testosterone in
375 the plasma of male mice: a difference between BALB/cBy and C57BL/6By inbred strains.
376 *J. Endocrinol.* **87**, 37–46 (1980).
377 18. Hill, D. J. & Milner, R. D. Insulin as a growth factor. *Pediatr. Res.* **19**, 879–886 (1985).
378 19. Crosby, P. *et al.* Insulin/IGF-1 Drives PERIOD Synthesis to Entrain Circadian Rhythms
379 with Feeding Time. *Cell* **177**, 896-909.e20 (2019).
380 20. Van Dycke, K. C. G. *et al.* Chronically Alternating Light Cycles Increase Breast Cancer
381 Risk in Mice. *Curr. Biol. CB* **25**, 1932–1937 (2015).
382 21. Blakeman, V., Williams, J. L., Meng, Q.-J. & Streuli, C. H. Circadian clocks and breast
383 cancer. *Breast Cancer Res. BCR* **18**, 89 (2016).
384 22. Zomer, A. *et al.* In Vivo imaging reveals extracellular vesicle-mediated phenocopying of
385 metastatic behavior. *Cell* **161**, 1046–1057 (2015).
386 23. van Rheenen, J. & Scheele, C. L. G. J. Intravital microscopy to illuminate cell state
387 plasticity during metastasis. *Curr. Opin. Cell Biol.* **72**, 28–35 (2021).
388 24. Kienast, Y. *et al.* Real-time imaging reveals the single steps of brain metastasis formation.
389 *Nat. Med.* **16**, 116–122 (2010).
390
391
392
393
394

395
396
397 **Main Figure Legends**
398
399 **Fig. 1: CTCs intravasate during the rest phase of the circadian rhythm.**
400 **a,** Graphical representation of the human circadian rhythm. The white and black bars represent
401 environmental light (active period) and dark conditions (rest period), respectively (*left*). The
402 radial histograms show the percent of single CTCs, CTC clusters and CTC-WBC clusters
403 isolated during the rest or active phase in early- or late-stage breast cancer patients. *n*=21 early-
404 stage and *n*=9 late-stage patients. **b,** Graphical representation of the mouse circadian rhythm.
405 The white and black bars represent environmental light (rest period) and dark conditions (active
406 period), respectively (*top*). Time kinetic analysis showing CTC counts in the NSG-CDX-BR16
407 breast cancer mouse model, from blood collected via cardiac puncture or tumor draining vessel
408 (TDV) over a 24-hour time period (*n*=4 for all time points, except ZT12 (cardiac puncture and
409 TDV) and ZT20 (TDV) where *n*=3). **c,** Box plots showing the distribution of the number of
410 CTCs collected at ZT4 or ZT16 in immunocompromised NSG-LM2 (*n*=6; single CTCs
411 *P*=0.0152; CTC clusters and CTC-WBC clusters *P*=0.0087) and NSG-4T1 (*n*=4; *P*=0.0286 for
412 all) or immunocompetent BALB/c-4T1 (*n*=5; single CTCs *P*=0.0159; CTC clusters *P*=0.0079;
413 CTC-WBC clusters *P*=0.0317) breast cancer mouse models. **d,** Graphical representation of
414 physiological (BL/6-EO771.lmb mice) *versus* impaired circadian rhythm (BL/6-*Bmal1*$^{-/-}$-
415 EO771.lmb mice) (*left*). Graphs showing time kinetic analysis of CTC counts (single CTCs,
416 CTC clusters and CTC-WBC clusters) in the BL/6-EO771.lmb (ZT4, ZT12, ZT16 *n*=4; ZT0
417 *n*=3) and BL/6-*Bmal1*$^{-/-}$-EO771.lmb (*n*=3) mice, from blood collected via cardiac puncture
418 over a 24-hour time period. Data in panel "b" and "d" are presented as mean ± s.e.m.; for panels
419 "c" center lines in the box represent the median; box limits represent first and third quartile;
420 extremes of the whisker lines represent the minimum and maximum observed values. * $P <$
421 0.05, ** $P < 0.01$ by two-sided Mann-Whitney test. *n* represents the number of biologically
422 independent mice.
423
424
425 **Fig. 2: The metastatic potential of CTCs is highest during the rest phase.**
426 **a,** Schematic illustration of the experimental design for panels "b" and "c". Equal numbers of
427 spontaneously shed ZT4-generated GFP-labelled CTCs and ZT16-generated RFP-labelled
428 CTCs from NSG-LM2 mice were co-injected *via* the tail vein into tumor free recipient mice at
429 different timepoints of the circadian rhythm (ZT0, ZT4, ZT12, ZT16) to measure their direct
430 metastatic ability. **b,** Representative bioluminescence images of lungs from mice being co-
431 injected simultaneously with ZT4-generated GFP-labelled CTCs and ZT16-generated RFP-
432 labelled CTCs from NSG-LM2 mice (*top*). The plot shows normalized bioluminescence signal
433 obtained from lungs of mice used in the same panel (*bottom*) (*n*=3). **c,** Representative
434 immunofluorescence images of GFP and RFP in lungs of mice shown in "b" (*left*). The plot
435 shows GFP and RFP levels in lungs of mice used in the same panel (*right*) (*n*=3; ZT4 *P*=0.0406;
436 ZT12 $P < 0.0001$). Scale bar = 100 μm. **d,** Schematic illustration of the experimental design
437 for panel "e". Single CTCs, CTC clusters and CTC-WBC clusters are collected at ZT4 or ZT16

438 and separately injected in the tail vein of recipient tumor-free mice to measure their direct
439 metastatic potential. **e,** Representative bioluminescence images of lungs from mice injected
440 with single CTCs, CTC clusters or CTC-WBC clusters collected at ZT4 or ZT16 from NSG-
441 LM2 mice (*top*). The plot shows normalized bioluminescence signal obtained from lungs of
442 mice used in the same panel (*bottom*) (*n*=3 for ZT4 single CTCs and CTC clusters; *n*=4 for
443 ZT16 single CTCs and CTC clusters; *n*=2 for CTC-WBC clusters, due to their rarity.
444 *P*=0.0272). For all panels, data are presented as mean ± s.e.m.; * $P < 0.05$, *** $P < 0.001$ by
445 unpaired two-sided t-test. *n* represents the number of biologically independent mice.
446
447
448 **Fig. 3: Rest phase CTCs are highly proliferative.**
449 **a,** Illustration of the experimental design. CTCs are collected at ZT4 or ZT16, then directly
450 processed for single cell RNA sequencing (scRNA-seq). **b,** Plot showing the principal
451 components PC4 and PC5 of gene expression in CTCs from NSG-CDX-BR16 mice. *Upper*
452 and *right* panels show the density of values for active (*blue*) and rest phase (*red*). **c,** Heatmap
453 showing row-normalized abundance of differentially-expressed genes between rest and active
454 phase in CTCs from NSG-BR16-CDX mice. **d,** Heatmap showing the pair-wise similarity of
455 enriched gene sets in CTCs of rest and active phase from NSG-CDX-BR16 mice. The heatmaps
456 on the *right* represent the adjusted GSEA *P* value and normalized enrichment score (NES). **e,**
457 Plot comparing the GSEA results (NES and *P* value) in NSG-CDX-BR16 (*left*) and NSG-LM2
458 (*right*) for gene sets shown in "d". **f,** Illustration of the experimental design. CTCs were
459 collected from breast cancer patients during the rest (04:00 am) or active phase (10:00 am),
460 then directly processed for scRNA-seq. The bar on the *top* represents environmental light
461 (*white*) and dark (*black*) phases. *Right* panel represent the GSEA results in patient CTCs as
462 described in "e". **g,** Average GSVA score for translation (*yellow*, *n*=5) and cell division (*blue*,
463 *n*=17) gene sets in CTCs from the NSG-LM2 time-kinetics experiment (ZT0 *n*=3, ZT4 *n*=3,
464 ZT12 *n*=3, ZT16 *n*=3, ZT20 *n*=3). Background represents environmental light (*white*) and dark
465 (*grey*) conditions. **h,** Representative immunofluorescence images of Ki67 and Pan-CK in
466 primary tumors from NSG-LM2 mice dissected at ZT0, ZT4, ZT12, ZT16, ZT20 (*n*=3;
467 *P*=0.002). Scale bar = 100 μm (*left*). Plot showing the intensity of Ki67 in tumors of NSG-
468 LM2 mice during different timepoints (*right*). Data are presented as mean ± s.e.m.; ** $P < 0.01$
469 by unpaired two-sided t-test. *n* represents the number of biologically independent mice.
470
471
472 **Fig. 4: Dexamethasone, testosterone and insulin regulate CTC intravasation.**
473 **a,** Schematic illustration of the expression of three key receptors (insulin receptor,
474 glucocorticoid receptor and androgen receptor) on breast cancer cells, activated by their
475 circadian rhythm-regulated ligands (insulin, glucocorticoid and testosterone, respectively)
476 during the active phase. **b,** Box plots showing the distribution of the number of single CTCs,
477 CTC clusters and CTC-WBC clusters isolated from mice treated with dexamethasone (4mg/kg)
478 or vehicle (0.03% DMSO) at ZT4 (*n*=4; *P*=0.0286 for all). **c,** Box plots showing the
479 distribution of the number of single CTCs (*P*=0.0159), CTC clusters (*P*=0.0317) and CTC-
480 WBC clusters (*P*=0.0159) isolated from testosterone-treated (*n*=5) or untreated mice (*n*=4) at

481 ZT4. **d,** Box plots showing the distribution of the number of single CTCs (ZT4 P=0.0002;
482 ZT16 P=0.0007), CTC clusters (ZT4 P=0.0002; ZT16 P=0.0153) and CTC-WBC clusters
483 (ZT4 P=0.0011; ZT16 P=0.0053) isolated from mice treated with insulin (0.7U/kg) or vehicle
484 (PBS) at ZT4 or ZT16 (n=8, except insulin-treated mice at ZT16 with n=6). **e,** Representative
485 immunofluorescence images of Ki67 and Pan-CK in primary tumors from control or insulin-
486 treated mice, dissected at ZT4 or ZT16 (n=4 except control mice at ZT4 with n=3). Scale bar
487 = 100 µm. **f,** Pie charts displaying the mean percent of Ki67 intensity in tumors shown in "e".
488 The NSG-LM2 model was used for all treatments. For panels "b", "c" and "d": the white and
489 black bars on the horizontal axis represent environmental light and dark conditions,
490 respectively; the grey arrows indicate treatment timing; center lines in the box represent the
491 median; box limits represent first and third quartile; extremes of the whisker lines represent the
492 minimum and maximum observed values. * $P < 0.05$, ** $P < 0.01$, *** $P < 0.001$ by two-sided
493 Mann-Whitney test. n represents the number of biologically independent mice.
494
495
496 **Methods**
497
498 *Patient samples*
499 All patients gave their informed written consent to participate in the study that took place at
500 the University Hospital Basel under the Clinical Research Protocol (#2020-00014) approved
501 by the Swiss authorities (EKNZ, Ethics Committee northwest/central Switzerland) and in
502 compliance with the Declaration of Helsinki. All patients were hospitalized and were either
503 temporarily off-treatment (patients with stage IV disease) or before operation (patients with
504 stage I-III disease) at the time of blood sampling. 7.5 ml of peripheral blood was collected from
505 breast cancer patients during the rest (04:00 am) and active (10:00 am) phase of the same day
506 in EDTA vacutainers. The time point for each sample collection was strictly followed.
507
508 *Cell culture*
509 Human CTC-derived BR16 cells were generated as previously described[25] from a patient with
510 hormone receptor-positive breast cancer at the University Hospital Basel and propagated as
511 suspension cultures in a humidified incubator at 37 °C with 5% O_2 and 5% CO_2. MDA-MB-
512 231 LM2 human breast cancer cells (obtained from J. Massagué, Memorial Sloan Kettering
513 Cancer Center), E0771.lmb mouse breast cancer cells (obtained from Robin Anderson, Olivia
514 Newton-John Cancer Research Institute) and 4T1 mouse breast cancer cells (ATCC) were
515 grown in DMEM medium (Gibco, 11330-057) supplemented with 10% FBS (Gibco,
516 10500064) in a humidified incubator at 37 °C with 20% O2 and 5% CO2. LM2, BR16 and 4T1
517 cells were transduced with lentiviruses carrying either GFP-luciferase or mCherry-luciferase.
518 Cell lines did not belong to the list of commonly misidentified cell lines (International Cell
519 Line Authentication Committee) and confirmed negative for mycoplasma contamination.
520 Authentication is not applicable for human CTC-derived BR16, MDA-MB-231 LM2 human
521 breast cancer cells variant, and E0771.lmb mouse breast cancer variant. 4T1 mouse breast
522 cancer cells were authenticated by Multiplexion GmbH. Finally, for the *in vivo* mouse
523 immunocompetent experiments, 4T1 and E0771.lmb cells were transduced with lentiviruses
524 carrying CD90.1.

525
526 *Mouse experiments*
527 All mouse experiments were carried out according to institutional and cantonal guidelines
528 (approved mouse protocol #3053, cantonal veterinary office of Basel-City and approved mouse
529 protocol #33688, cantonal veterinary office of Zurich). Experiment endopoints that were
530 allowed in our approved license included tumor-related factors such as a maximum tumor size
531 of 2'800 mm^3 or severe ulceration, as well as appearance and behavior features such as
532 hunching, piloerection or decreased activity. These limits were not exceeded in any of the
533 experiments. Sample size calculations were not predetermined, but number of animals were
534 chosen to comply with the 3R principles. All mice were randomized before the start of each
535 experiment, but blinding was not performed. NSG (NOD-scid-Il2rgnull) (The Jackson
536 Laboratory), BALB/c (Janvier Labs) and C57BL/6J (The Jackson Laboratory) female mice
537 were kept in pathogen-free conditions, accordingly to institutional guidelines. *Bmal*1 knockout
538 mice (C57BL/6J background) were purchased and genotyped from the The Jackson
539 Laboratory. Animals were kept in a standard light cycle photoperiod (12 hrs light:12 hrs dark;
540 12:12 LD) with ZT0 defined as lights on (06.00 am) and ZT12 as lights off (06.00 pm). For the
541 20-t and 28-t cycle studies, animals were kept in 10:10 LD or 14:14 LD cycle conditions,
542 respectively. Orthotopic breast cancer lesions were generated in 8-week-old NSG females upon
543 the injection with either 1×10^6 LM2-mCherry-Luciferase cells (NSG-LM2 model),
544 1×10^6 BR16-GFP-Luciferase cells (NSG-CDX-BR16 model) or 0.5×10^6 4T1-GFP-
545 Luciferase cells (NSG-4T1 model) into the mammary fat pad. Similarly, 0.5×10^6 4T1-
546 CD90.1 cells were orthotopically injected into the mammary fat pad of 8-week-old BALB/c
547 female mice (BALB/c-4T1 model). Finally, 1×10^6 E0771.lmb-CD90.1 cells were
548 orthotopically injected into the mammary fat pad of 8-week-old WT (BL/6-E0771.lmb model)
549 or *Bmal1* knockout mice (BL/6-*Bmal1*$^{-/-}$-E0771.lmb model). In all cases, breast cancer cells
550 were inoculated in 100 µl of 50% Cultrex PathClear Reduced Growth Factor Basement
551 Membrane Extract (R&D Biosystems, 3533-010-02) in PBS. Blood draw for CTC analysis,
552 organ dissection and IVIS bioluminescence imaging were performed during the rest or active
553 phase after 4.5 weeks for NSG-LM2, 4 weeks for NSG-4T1 and BALB/c-4T1, 3 weeks
554 for BL/6- $^{-}$-E0771.lmb and BL/6-*Bmal1*$^{-/-}$-E0771.lmb and 5-to-6 months for NSG-CDX-BR16
555 mice. The time point for each sample collection was strictly followed. All mice were
556 randomized before mouse experiments and blindly selected before injection. Maximal
557 approved tumor volume was never exceeded.
558
559 *Mouse treatments*
560 1×10^6 LM2-mCherry-Luciferase cells were orthotopically injected into the mammary fat pad
561 of 8-week-old NSG female mice. Upon tumor development, mice were treated with different
562 circadian-regulated hormones based on their pharmacokinetics profiles and the possibility of
563 developing negative regulatory loops upon prolonged treatment. For melatonin, treatments
564 started 10 days after the tumor injection, when tumors started growing exponentially and CTCs
565 were not yet detectable in peripheral blood. Mice were treated daily with melatonin (20 mg/kg;
566 Sigma-Aldrich, M5250-1G) alone or in combination with Luzindole (5 mg/kg; Sigma-Aldrich,
567 L2407). Luzindole treatments were performed 30 min before melatonin, which was
568 administrated 1.5 hr before the onset of the rest phase (ZT0). Blood collection and CTC

569 analysis was performed at ZTO. For dexamethasone, mice were treated with dexamethasone
570 (4mg/kg; Sigma-Aldrich, D1159-500MG) once 2 hours before the blood collection (ZT4) to
571 avoid the activation of the negative regulatory loop of the HPA axis[26]. For testosterone, mice
572 were injected with testosterone implants (Belma Technologies, T-M/60) 4 days before the
573 tumor injection. Implants were kept till the day of the blood collection (ZT4). For insulin,
574 treatments started 25 days after the tumor cell injection to avoid an effect of insulin on tumor
575 growth. Mice were treated daily with insulin (0.7U/kg; Humalog) in parallel with glucose
576 (1g/kg; Sigma-Aldrich, G7021) at ZT3. Blood collection and CTC analysis was performed at
577 ZT4 and ZT16. All treatments were performed as intraperitoneal (IP) injections in a final
578 volume of 100 µl.
579
580 *Jet lag experiment*
581 1×10^6 LM2-mCherry-Luciferase or 0.5×10^6 4T1-GFP-Luciferase cells were orthotopically
582 injected into the mammary fat pad of 8-week-old NSG female mice. Jet lag was initiated one
583 week after the tumor injection by placing the animals in altered light-cycle conditions with an
584 8-hr light advance every 2-3 days[9]. Melatonin treatments in jet lagged mice were performed
585 daily, 1.5 hr before the onset of each jet lagged rest phase. Blood collection and CTC analysis
586 was performed at the onset of the rest phase.
587
588 *CTC capture*
589 For patient samples, 7.5 ml of peripheral blood was processed for microfluidic-based CTC
590 capture within 1 hr from blood draw. Using the Parsortix Cell Separation System (ANGLE,
591 plc), CTCs were captured in Cell Separation cassettes (GEN3D6.5) and then stained with an
592 antibody cocktail containing EpCAM-AF488 (Cell Signaling Technology, CST5198), HER2-
593 AF488 (BioLegend, 324410), EGFR-FITC (GeneTex, GTX11400) and CD45-BV605
594 (BioLegend, 304042). For mouse experiments, 0.8 ml of blood was collected via cardiac
595 puncture and processed immediately. For the immunocompromised models, samples were
596 stained only for CD45, as cancer cells were identified on the basis of mCherry or GFP
597 expression. For the immunocompetent models, an anti-CD45 staining was performed in
598 parallel with staining for CD90.1 (OX-7 clone, BioLegend, 202508) to identify WBC and
599 cancer cells, respectively. The number of captured CTCs, including single CTCs, CTC clusters
600 and CTC-WBC clusters, was determined while cells were still in the cassette. CTCs were then
601 released from the cassette in DPBS (Gibco,14190169) onto ultra-low attachment plates
602 (Corning, 3471-COR) for futher downstream analysis.
603
604 *Direct metastatic potential assay*
605 1×10^6 LM2-mCherry-Luciferase, LM2-GFP-Luciferase or BR16-GFP-Luciferase cells were
606 orthotopically injected into the mammary fat pad of 8-week-old NSG female mice. Upon tumor
607 development, blood was collected via heart puncture at ZT4 or at ZT16, run through the
608 Parsortix system and captured CTCs were released onto ultra-low attachment plates. Using the
609 CellCelector, an automated single-cell picking system (ALS), single CTCs, CTC clusters and
610 CTC-WBC clusters were individually micromanipulated and then each category was injected
611 into the tail vein of recipient NSG mice. Metastasis onset and growth rate in lungs was non-
612 invasively monitored on a weekly schedule with the IVIS bioluminescence system. The

613 experiment was terminated 4-months post injection of LM2-mCherry-Luciferase and LM2-
614 GFP-Luciferase cells or 5-months post injection of BR16-GFP-Luciferase CTCs cells.
615
616
617 *Immunofluorescence staining and confocal analysis*
618 Dissected organs and primary tumours were fixed in 4% PFA at 4^0C overnight. After paraffin
619 embedding, the Thermo Scientific Rotary Microtome Microm HM 355S was used to cut slices
620 of 7 μm of thickness. Following a standard deparaffinization/antigen retrieval protocol,
621 samples were stained for pan-CK (1:65; GeneTex, GTX27753), Ki67 (1:250; Abcam,
622 ab15580), GFP (D5.1; 1:200; Cell Signaling Technology, 2956), mCherry (16D7; 1:300:
623 Invitrogen, M11217) and DAPI (1µg/ml; Sigma-Aldrich, D9542-1MG). CTCs were
624 cytocentrifuged onto microscope slides and fixed in 4% PFA. Post-fixation, cells were washed
625 with PBS, permeabilized for 5 min in 0.5% TritonX-100/PBS and blocked with 5% BSA in
626 0.1% Triton/PBS for 1 hr before Ki67 (1:250; Abcam, ab15580), TAZ (1:100; BD Biosciences,
627 560235), YAP (D8H1X; 1:1000; Cell Signaling Technology, 14074) or cleaved-caspase3
628 (5A1E; 1:100; Cell Signaling Technology, 9664) antibody was added. Immunofluorescence
629 imaging was performed on a Leica SP5 confocal microscope and images were taken using the
630 60x oil lens. All images were analyzed by the Fiji image processing software (2.1.0/1.53c).
631
632 *Flow cytometry*
633 Mouse tumours were minced in fragments and enzymatically digested for 15 minutes with 2
634 mg/ml type IV Collagenase plus 50 U/ml bovine DNase. The digested tumours were
635 mechanically dissociated in C-tubes using a GentleMACS device (Miltenyi), then subjected to
636 red blood cell lysis using ACK Buffer (Lonza) and immediately stained. Whole mouse blood
637 was pelleted and red blood cells were lysed using ACK Buffer and immediately stained. For
638 immunostaining, cells were blocked in a 2% FCS solution containing 2 mM
639 Ethylenediaminetetraacetic acid (EDTA) and FcR blocking reagent (Miltenyi). Mouse
640 peripheral blood cells were stained with the following antibodies: Alexa Fluor® 594 anti-
641 mouse Ly-6G (1:500; 1A8 clone, BioLegend, 127602), Alexa Fluor® 594 anti-mouse CSF-
642 1R/CD115 (1:200; AFS98 clone, BioLegend, 135520), APC/Cyanine7 anti-CD11b Antibody
643 (1:500; M1/70 clone, BioLegend, 101226), Brilliant Violet 421™ anti-mouse CD3 (1:200;
644 17A2 clone, BioLegend, 100228), PE anti-mouse NKp46/CD335 (1:100; 29A1.4 clone,
645 BioLegend, 137647), Alexa Fluor® 647 anti-mouse CD49b (1:200; DX5 clone, BioLegend,
646 103511), Alexa Fluor® 488 anti-mouse CD8a (1:200; 53-6.7 clone, BioLegend, 100723),
647 Brilliant Violet 510™ anti-mouse CD4 (1:500; GK1.5 clone, BioLegend, 100449), PE anti-
648 mouse CD223/LAG-3 (1:100; C9B7W clone, BioLegend, 125224). Dissociated tumour cells
649 were stained with the above-mentioned antibodies plus CD90.1 (1:500; OX-7 clone,
650 BioLegend, 202508) to distinguish CD90.1-labeled cancer cells from the infiltrating stroma.
651 All samples were processed on an LSR Fortessa device (BD) and further analysed with FlowJo
652 (Tree Star).
653
654 *Single-cell RNA sequencing*
655 Using the CellCelector, an automated single-cell picking system (ALS), single CTCs, CTC
656 clusters and CTC-WBC clusters were collected and immediately transferred into individual

657 tubes (Axygen, 321-032-501) containing 2.5 µl RLT Plus lysis buffer and 1U SUPERase IN
658 RNase inhibitor (Invitrogen, AM2694). Samples were immediately frozen and kept at
659 80^{0}C until further processing. Amplified cDNA was prepared according to the Smart-seq2
660 protocol. Libraries were prepared using with Nextera XT (Illumina) and sequenced on Illumina
661 NextSeq500 instrument in 75-bp single-read mode. This yielded a median raw sequencing
662 depth of 1.64 million reads per sample.
663
664 *RNA-sequencing analysis*
665 Sequencing reads were quality-trimmed with Trim Galore! (v0.6.5,
666 https://www.bioinformatics.babraham.ac.uk/projects/trim_galore/; parameters:–q 20 –length
667 20) and Cutadapt (v3.4). Quality assessment of RNA-seq data was performed using FastQC
668 (v0.11.4, https://www.bioinformatics.babraham.ac.uk/projects/fastqc), FastQ Screen (v0.11.4,
669 https://www.bioinformatics.babraham.ac.uk/projects/fastq_screen/) and visualized with
670 MultiQC (v1.7). Trimmed reads were aligned to human (GRCh38) genome reference using
671 STAR (v.2.7.3a; parameters: --twopassMode Basic --outSAMmapqUnique 60 --sjdbGTFfile)
672 with splice junctions from the human GENCODE annotation (release 35). To eliminate
673 residual contamination from mouse RNA, reads derived from xenograft models were also
674 aligned to mouse (GRCm38) genome reference using STAR (v.2.7.3a; parameters: --
675 twopassMode Basic --outSAMmapqUnique 60 --sjdbGTFfile), with splice junctions from the
676 mouse GENCODE annotation (release M25) and assigned to either human or mouse using
677 Disambiguate (v1.0.0). Resulting BAM files were sorted by Samtools (v1.10) and the
678 alignment quality evaluated using RSeQC (v.2.6.4). The gene-level expression counts were
679 computed with featureCounts (v.2.0.1; parameters: -t exon -g gene_id --minOverlap 10 -Q 10)
680 using the human gene annotations from GENCODE (release 35). Genes present with at least 3
681 reads in 50% of the samples were kept for the analysis. Single cell samples were retained for
682 further analyses if they had at least 50,000 reads, at least 5,000 genes with non-zero expression
683 and having less than 50% of reads mapping to mitochondrial genes. For samples containing
684 more than 1 cell (CTC clusters and CTC-WBC clusters), the minimum number of genes was
685 set to 8,000. Read counts were normalized using the TrimmedMean of M-values (TMM)
686 method implemented in the R/bioconductor package edgeR (v3.34.1). Quality control and
687 visualization of processed data was performed with the help of the R/Bioconductor scater
688 package (v1.20.1). After normalization, principal component analysis (PCA) was conducted
689 using gene expression (log_2 normalized counts) of the top 500 genes with the largest biological
690 components according to getTopHVGs function from R/bioconductor package scran (v1.20.1).
691 Selected PCs were associated to technical and biological variables using Pearson correlation.
692 The number of PCs selected was defined by the elbow method.
693
694 *Differential expression and gene set enrichment analyses*
695 Differential expression (DE) analysis was computed with the quasi-likelihood (QL) approach
696 from edgeR R/bioconductor package (v3.34.1) using robust dispersion estimates. Prior to DE
697 analysis, genes detected in less than 50% of smallest group sample size were removed from
698 the analysis (threshold 5 counts per million (CPM)). *P* values were adjusted for multiple
699 comparisons using the Benjamini–Hochberg method. Gene set enrichment analysis (GSEA)
700 was conducted with the Fast GSEA (FGSEA) method implemented in the R/Bioconductor

701 package clusterProfiler (v4.0.5). As input for GSEA we used a list of genes ranked by fold-
702 change and two gene set collections from the Molecular Signatures Database (MsigDB, v7.4):
703 C2 canonical pathways and C5 GO Biological Process. FGSEA performs a preliminary
704 estimation of enrichment *P* values using permutation test (1000 permutations) and a secondary
705 estimation of low *P* values using the multilevel algorithm with $1e^{-10}$ boundary. An adjusted *P*
706 value cut-off of 0.0001 was applied to define enriched gene sets. Only gene sets with a size
707 between 10 and 500 genes were included in the analysis. The Jaccard coefficient was computed
708 to measure the similarity between the enriched terms using the genes included in the GSEA
709 leading-edge subset within each gene set. In NSG-LM2 and patients the GSEA analysis was
710 performed using only the enriched terms from the NSG-CDX-BR16 model. Gene Set Variation
711 Analysis (GSVA) was conducted with the R/Bioconductor GSVA package to obtain sample
712 level enrichment scores for the same MSigDB collections evaluated in the GSEA analysis.
713 Differences in enrichment score across the multiple time points were estimated using the
714 moderated F-statistic obtained through the empirical Bayes approach implemented in the
715 R/Bioconductor package limma v3.48.3). Time points with less than 3 replicates were removed
716 form this analysis.
717
718 *Data analysis*
719 Data analysis, statistical testing and visualization were conducted in Graphpad Prism (v.9.1.1),
720 R (version 4.1.0; R Foundation for Statistical Computing) and bioconductor (v.3.13). Figure
721 legends describe the statistical approach used for each analysis.
722
723 *Data availability*
724 RNA sequencing data have been deposited in the Gene Expression Omnibus (GEO, NCBI;
725 accession number GSE180097). Processed transcriptomics data, large data sets and additional
726 files required for reproducibility are available from the Zenodo data repository
727 (https://doi.org/10.5281/zenodo.6358987). Human reference genome (GRCh38), mouse
728 reference genome (GRCm38), human gene annotation (release 35) and mouse gene annotation
729 (release M25) were downloaded from GENCODE (https://www.gencodegenes.org). Gene sets
730 were downloaded from the Molecular Signatures Database (MsigDB, v7.4, http://www.gsea-
731 msigdb.org/gsea/msigdb/collections.jsp). All data are available from the corresponding author
732 upon reasonable request.
733
734 *Code availability*
735 Code related to the data analysis of this study has been deposited to GitHub (accession URL,
736 https://github.com/TheAcetoLab/diamantopoulou-ctc-dynamics) and archived at Zenodo
737 (https://doi.org/10.5281/zenodo.6484917). Descriptions of how to reproduce the analysis
738 workflows showing code, R packages version numbers and final figures presented in this paper,
739 are available at https://theacetolab.github.io/diamantopoulou-ctc-dynamics. All data are
740 available from the corresponding author upon reasonable request.
741
742
743 9. Papagiannakopoulos, T. *et al.* Circadian Rhythm Disruption Promotes Lung
744 Tumorigenesis. *Cell Metab.* **24**, 324–331 (2016).

25. Yu, M. *et al.* Cancer therapy. Ex vivo culture of circulating breast tumor cells for individualized testing of drug susceptibility. *Science* **345**, 216–220 (2014).
26. Jones, M. T., Hillhouse, E. W. & Burden, J. L. Dynamics and mechanics of corticosteroid feedback at the hypothalamus and anterior pituitary gland. *J. Endocrinol.* **73**, 405–417 (1977).

Acknowledgments

We thank all patients that donated blood for our study, as well as involved clinicians and study nurses. We thank members and collaborators of the Aceto lab for scientific feedback and discussions. We thank J. Massagué (Memorial Sloan Kettering Cancer Center) for donating LM2 breast cancer cells; R. Anderson (Olivia Newton-John Cancer Research Institute) for donating E0771.lmb mouse breast cancer cells; the Genomics Facility Basel (D-BSSE of the ETH Zurich) for generating libraries and performing next-generation sequencing; P. Lorentz (University of Basel) for microscopy support; A. Offinger (University of Basel) with her team as well as the EPIC team (ETH Zurich) for support with animal work; M. Sonderegger-Stalder and Kristina Degener (Cantonal Hospital Basel-Land) for support with clinical samples. Research in the Aceto laboratory is supported by the European Research Council (#101001652), the strategic focus area of Personalized Health and Related Technologies at ETH Zurich (#PHRT-541), the Future and Emerging Technologies programme of the European Commission (grant 801159-B2B), the Swiss National Science Foundation (#PP00P3_190077), the Swiss Cancer League (#KLS-4834-08-2019), the Basel Cancer League (#KLbB-4763-02-2019), the two Cantons of Basel through the ETH Zürich (#PMB-01-16), the University of Basel and the ETH Zürich. Z. Diamantopoulou is a H2020 Marie Skłodowska-Curie Actions (#101028567) Fellow.

Authors contributions

Z.D. and N.A. designed the study, performed the experiments and wrote the manuscript. F.C.-G. performed the computational analysis. M.S. generated the 4T1-CD90.1 cells and performed the immune cell analysis. S.B. performed immunofluorescence staining. K.S. contributed to mouse experiments and processed mouse tissues. I.K. processed blood samples. F.S., C.F., B.S., M.V., C.R., W.P.W., C.K. and V.H.-S., provided patient samples. All authors have read, commented and approved the manuscript in its final form.

Competing interests

N.A. is co-founder and member of the board of PAGE Therapeutics AG, Switzerland, listed as inventor in patent applications related to CTCs and a paid consultant for companies with an interest in liquid biopsy. All other authors declare no competing interests.

789
790
791
792
793
794 **Additional information**
795
796 **Supplementary information** The online version contains supplementary material available
797 at XXX
798 **Correspondence and requests for materials** should be addressed to Nicola Aceto.
799 **Peer review information** *Nature* thanks XXX and the other, anonyomous, reviewer(s) for
800 their contribution to the peer review of this work.
801 **Reprints and permissions information** is available at XXX
802
803
804
805
806 **Extended Data Figure Legends**
807
808 **Extended data Fig. 1: Tumor size and CTCs intravasation rates during different phases**
809 **of the circadian rhythm.**
810 **a,** Pie charts displaying the mean percent of total CTCs, single CTCs, CTC clusters and CTC-
811 WBC clusters detected during the rest or active phase in breast cancer patients (*n*=30), in NSG-
812 LM2 mice (*n*=6), NSG-CDX-BR16 mice (*n*=6), NSG-4T1 mice (*n*=4) or BALB/c-4T1 mice
813 (*n*=6). **b,** Time kinetic analysis showing mean CTC counts in the NSG-LM2 (*n*=3), NSG-4T1
814 (*n*=3) and BALB/c-4T1 (ZT0, ZT4, ZT20 *n*=3; ZT12, ZT16 *n*=4) breast cancer mouse models
815 over a 24-hour time period. Data are presented as mean ± s.e.m. **c,** Plots showing the size of
816 the primary tumors dissected at different timepoints from NSG-CDX-BR16 mice (ZT0, ZT4,
817 ZT16, ZT20 *n*=4; ZT12 *n*=3), NSG-LM2 (*n*=3), NSG-4T1 mice (*n*=3) and BALB/c-4T1 (ZT0,
818 ZT4, ZT20 *n*=3; ZT12, ZT16 *n*=4) mice. Data are presented as mean ± s.e.m. **d,** Representative
819 bioluminescence images of lungs from NSG-CDX-BR16, NSG-LM2 and NSG-4T1 mice taken
820 at different timepoints (ZT0, ZT4, ZT12, ZT16, ZT20) (*n*=3). **e,** Box plots showing the
821 distribution of the number of single CTCs (*P*=0.0043), CTC clusters (*P*=0.0087) and CTC-
822 WBC clusters (*P*=0.0130) collected at ZT4 or ZT16 in the NSG-CDX-BR16 mouse model
823 (*n*=6). Center lines in the box represent the median; box limits represent first and third quartile;
824 extremes of the whisker lines represent the minimum and maximum observed values. Data are
825 presented as mean ± s.e.m.; * $P < 0.05$, ** $P < 0.01$ by two-sided Mann-Whitney test. **f,** Plots
826 showing the size of primary tumors from NSG-CDX-BR16 (n=6), NSG-LM2 (*n*=6), NSG-4T1
827 (*n*=4) and BALB/c-4T1 (*n*=5) mice dissected at ZT4 or ZT16. Data are presented as mean ±
828 s.e.m. **g,** Plots showing the mean fold change increase of CTC counts isolated at ZT4 or ZT16
829 from NSG-LM2, NSG-CDX-BR16, NSG-4T1 and BALB/c-4T1 mice. **h,** Pie charts displaying
830 the mean percentage of single CTCs, CTC clusters and CTC-WBC clusters detected during the
831 rest or active phase in patients (*n*=7), NSG-LM2 (*n*=6), NSG-CDX-BR16 (*n*=6), NSG-4T1
832 (*n*=4) or BALB/c-4T1 (*n*=6) mice. For all panels, *n* represents the number of biologically
833 independent mice.

834
835
836 **Extended data Fig. 2: The abundance of CTCs during the rest phase is due to increased**
837 **intravasation.**
838 **a,** Box plots showing the distribution of the number of CTCs collected at ZT4 or ZT16 via
839 cardiac puncture or tumor draining vessel (TDV) in the NSG-CDX-BR16 breast cancer mouse
840 model (n=4; P=0.0286 for all). **b,** Representative bioluminescence images of lungs from NSG-
841 CDX-BR16 mice taken at different timepoints (ZT0, ZT4, ZT12, ZT16, ZT20) over a 24-hour
842 time period (n=4). **c,** Box plots showing the distribution of the number of CTCs collected at
843 ZT4 or ZT16 via cardiac puncture or TDV in the NSG-LM2 breast cancer mouse model (n=4;
844 P=0.0286 for all). **d,** Representative bioluminescence images of lungs from NSG-LM2 mice
845 taken at ZT4 or ZT16 (n=4). **e,** Plot showing the size of primary tumors dissected from NSG-
846 LM2 mice at ZT4 or ZT16 (n=4). **f,** Time kinetic analysis showing fold change differences in
847 the number of LM2 cells detected in the circulation after their intravascular inoculation at
848 different time points of the circadian rhythm (ZT0, ZT4, ZT12, ZT16) (n=3 except ZT4 where
849 n=4). **g,** Plots showing the percentage of CTC clearance at different time points of the circadian
850 rhythm (ZT0, ZT4, ZT12, ZT16) 5 minutes after intravascular inoculation of LM2 cells (n=3
851 except ZT4 where n=4). For panels "e", "f" and "g", data are presented as mean ± s.e.m. For
852 panels 'a' and "c", center lines in the box represent the median; box limits represent first and
853 third quartile; extremes of the whisker lines represent the minimum and maximum observed
854 values. * $P < 0.05$ by two-sided Mann-Whitney test. For all panels, n represents the number of
855 biologically independent mice.
856
857
858 **Extended data Fig. 3: Circadian rhythm and melatonin regulate the intravasation of**
859 **CTCs.**
860 **a,** Illustration of the experimental design for "b" and "e". **b,** Box plots showing the mean
861 number of CTCs isolated from NSG-LM2 (n=5; single CTCs P=0.0079, CTC clusters
862 P=0.0079, CTC-WBC clusters P=0.0317) and NSG-4T1 (n=4; P=0.0286 for all) mice that
863 were kept in standard light cycle conditions (12:12, LD) or being jet-lagged. The blood draw
864 was performed at ZT4. **c,** Plots showing the mean fold change decrease of CTC counts upon
865 jet lag in NSG-LM2 (n=5) and NSG-4T1 (n=4) mice shown in "b". **d,** Plots showing the size
866 of primary tumors dissected from NSG-LM2 (n=5) and NSG-4T1 (n=4) mice shown in "b".
867 Data are presented as mean ± s.e.m. **e,** Box plots showing the distribution of the number of
868 CTCs isolated from NSG-LM2 mice that were being jet-lagged (*left*) or kept in standard light
869 cycle conditions (*right*) and were treated with melatonin alone or in combination with its
870 antagonist luzindole. The blood draw was performed at ZT4 or ZT0. (n=4, except control and
871 melatonin-treated mice in combination with luzindole at ZT4 where n=5; ZT4 P=0.0159 except
872 CTC-WBC clusters treated with melatonin in combination with lunzindole where P=0.0317;
873 ZT0 P=0.0286 except single CTCs treated with melatonin in combination with lunzindole
874 where P=0.0091). **f,** Plots showing the size of primary tumors dissected from mice shown in
875 "e". Data are presented as mean ± s.e.m. **g,** Representative bioluminescence images of lungs
876 from NSG-LM2 mice that were kept in standard light cycle conditions (12:12, LD) and were

877 treated with melatonin alone or in combination with luzindole. For panels 'b' and "e", center
878 lines in the box represent the median; box limits represent first and third quartile; extremes of
879 the whisker lines represent the minimum and maximum observed values. * $P < 0.05$, ** $P <$
880 0.01 by two-sided Mann-Whitney test. For all panels, *n* represents the number of biologically
881 independent mice.
882
883
884 **Extended data Fig. 4: Light exposure impacts CTC intravasation.**
885 **a,** Time kinetic analysis showing mean CTC counts (single CTCs, CTC clusters and CTC-
886 WBC clusters) in the NSG-LM2 mice kept in altered light-dark (LD) cycles (LD 14:10, *n*=3;
887 LD 10:10, *n*=4, except ZT10 and ZT20 where *n*=3; LD 14:14, *n*=4, except ZT14 where *n*=3).
888 **b,** Scatter dot plots showing the distribution of the number of single CTCs, CTC clusters and
889 CTC-WBC clusters isolated from NSG-LM2 mice that were kept in altered light cycles (LD
890 14:10, *n*=3; LD 10:10, *n*=4; LD 14:14, *n*=4; P =0.0286 for all). * $P < 0.05$ by two-sided Mann-
891 Whitney test. **c,** Plots showing the size of primary tumors dissected from NSG-LM2 mice
892 shown in "a". **d,** Representative bioluminescence images of lungs from NSG-LM2 mice shown
893 in "a". **e,** Graphs showing time kinetic analysis of CTC counts (single CTCs, CTC clusters and
894 CTC-WBC clusters) in the BL/6-EO771.lmb (ZT4, ZT12, ZT16 *n*=4; ZT0 *n*=3) and BL/6-
895 *Bmal1*$^{-/-}$-EO771.lmb (*n*=3) breast cancer mouse models collected via tumor draining vessel
896 (TDV) over a 24-hour time period. **f,** Plots showing the size of the primary tumors dissected
897 from BL/6-EO771.lmb and BL/6-*Bmal1*$^{-/-}$-EO771.lmb mice shown in Fig. 1d. **g,** Plotted
898 actograms showing the running activity of the BL/6-EO771.lmb and BL/6-*Bmal1*$^{-/-}$-
899 EO771.lmb mice with dark and light areas representing low and high activity, respectively. For
900 all panels, data are presented as mean ± s.e.m. *n* represents the number of biologically
901 independent mice.
902
903
904 **Extended data Fig. 5: Rest-phase CTCs have increased metastatic potential.**
905 **a,** Representative immunofluorescence images for Pan-CK in lungs of mice injected with
906 single CTCs, CTC clusters and CTC-WBC clusters collected at ZT4 or ZT16 from NSG-LM2
907 mice (ZT4 *n*=3 except CTC-WBC clusters *n*=2; ZT16 *n*=4 for all). Scale bar = 100 μm. **b,** Plot
908 showing the size of the metastatic lesions detected in the lungs of mice injected with single
909 CTCs, CTC clusters or CTC-WBC clusters collected at ZT4 or ZT16 of NSG-LM2 mice (ZT4
910 *n*=3 except CTC-WBC clusters *n*=2; ZT16 *n*=4 for all; P=0.0007). **c,** Representative
911 bioluminescence images of bones from mice injected with single CTCs, CTC clusters or CTC-
912 WBC clusters collected at ZT4 or ZT16 from NSG-CDX-BR16 mice. Mice were not injected
913 with CTC-WBC clusters collected during the active phase, due to their rarity. **d,** Plot showing
914 normalized bioluminescence signal obtained from bones of mice shown in panel "c" (single
915 CTCs *n*=4; CTC clusters *n*=5; P=0.006). **e**, Representative bioluminescence images of livers
916 from mice injected with single CTCs or CTC clusters, collected at ZT4 or ZT16 from NSG-
917 CDX-BR16 mice. Mice were not injected with CTC-WBC clusters collected during the active
918 phase, due to their rarity. **f,** Plot showing normalized bioluminescence signal obtained from
919 liver of mice shown in panel "e" (*n*=5 except single CTCs collected at ZT16 where *n*=4;

920 P=0.0301). For all panels, data are presented as mean ± s.e.m.; unpaired two-sided t-test * P < 0.05, ** P < 0.01, *** P < 0.001. n represents the number of biologically independent mice.
922
923
924 **Extended data Fig. 6: Time point of CTC isolation is the main determinant of gene**
925 **expression heterogeneity in CTCs.**
926 **a,** Heatmap showing the Pearson's correlation coefficient of PC1-7 eigenvectors from gene
927 expression with technical and biological variables in BR16-CDX CTCs. P values by two-sided
928 Pearson's correlation test (*P < 0.01, **P <0.001, ***P <0.0001). **b,** Scatter plot showing the
929 correlation of the fold-change between active and rest phase in single CTC (Y-axis) versus
930 CTC clusters and CTC-WBC (X-axis), using genes with $FDR \leq 0.05$ in any of the two sets
931 (two-sided Pearson's correlation coefficient 0.57, P value ≤ 2.22e-16). Points are colored
932 according to the dataset where they were found with a $FDR \leq 0.05$ (both, single CTC or CTC
933 clusters and CTC-WBC clusters). The dashed *red* line represents the linear regression line
934 using all the points in the plot. **c,** Bar plot showing the number of differentially expressed genes
935 (absolute $\log_2$ fold change ≥ 0.5 and $FDR \leq 0.05$) using all the samples ('All'), using clustered
936 CTCs (CTC clusters and CTC-WBC clusters) and using single CTCs. **d,** Heatmap showing the
937 pair-wise similarity matrix of enriched gene sets (gene set enrichment analysis (GSEA)
938 adjusted P value ≤ 0.001) using differential expression between CTCs of rest and active phase
939 from NSG-CDX-BR16 mice. Heatmap colors represent the Jaccard similarity coefficient using
940 the set of core genes in each gene set. The heatmap on the *right* represents the GSEA adjusted
941 P value. **e,** Plots comparing the normalized enrichment score (NES) and adjusted P value (dot
942 size) obtained using GSEA for gene sets shown in "d"**.** Gene sets with an adjusted P value ≤
943 0.05 in each sample set are highlighted in *red*. **f,** GSVA score for translation (*yellow*, n= 5) and
944 cell division (*blue*, n= 17) gene sets in CTCs obtained from the NSG-LM2 time-kinetics
945 experiment. *Yellow* and *blue* lines represent the average at each time point. Individual points
946 represent the enrichment score for each CTC sample. The *white* and *grey* backgrounds
947 represent environmental light (rest period) and dark conditions (active period), respectively.
948 Adjusted F-test P values as obtained from limma are shown for each individual gene set.
949
950
951 **Extended data Fig. 7: The proliferation status of primary tumours changes in a circadian**
952 **rhythm dependent manner.**
953 **a,** Representative immunofluorescence images of Ki67 and Pan-CK in primary tumors from
954 NSG-CDX-BR16 mice, dissected at different timepoints (ZT0, ZT4, ZT12, ZT16, ZT20) over
955 a 24-hour time period (ZT4, ZT12, ZT16 n=3; ZT0, ZT20 n=2; P=0.0270; scale bar = 100 μm)
956 (*left*). The plot shows the intensity of Ki67 in tumors of NSG-CDX-BR16 mice during different
957 timepoints (*right*). Data are presented as mean ± s.e.m.; unpaired two-sided t-test * P < 0.05.
958 **b,** Representative immunofluorescence images of Ki67 in CTCs collected at ZT4 and ZT16
959 from NSG-LM2 and NSG-CDX-BR16 mice. Scale bar = 10 μm. **c,** Plots showing the
960 distribution of Ki67 intensity in single CTCs (NSG-LM2 P=0.0495; NSG-CDX-BR16
961 P=0.0001) and CTC clusters (NSG-LM2 P=0.0223; NSG-CDX-BR16 P=0.0045) collected at
962 ZT4 and ZT16 from NSG-LM2 and NSG-CDX-BR16 mice (n=3). Box center lines in the box

963 represent the median; limits represent first and third quartile; extremes of the whisker lines
964 represent the minimum and maximum observed values. * $P < 0.05$, ** $P < 0.01$, *** $P < 0.001$
965 by two-sided Mann-Whitney test. For all panels, *n* represents the number of biologically
966 independent mice.
967
968
969 **Extended data Fig. 8: Breast cancer derived CTCs lack a functional circadian clock.**
970 **a,** Plot showing the expression distribution of core circadian genes in CTCs from NSG-CDX-
971 BR16 mice. The fold change (FC, in $\log_2$ scale) and adjusted *P* value from the global
972 differential expression analysis are shown for each gene. **b,** Density plot showing the
973 distribution of the average expression ($\log_2$ counts per million) of genes in CTCs from NSG-
974 CDX-BR16 mice. Core circadian genes are labeled in the X-axis. **c,** qPCR for *Bmal1*
975 expression in the liver, adrenal glands and primary tumor of NSG-LM2 mice (*n*=3 for all the
976 time points of the adreanal glands; *n*=3 for all the time points of the liver and tumor, except
977 ZT4 and ZT20 where *n*=4). Data are relative to the time point with the lowest expression levels
978 of *Bmal1* (ZT16; set as 1) and are presented as mean ± s.e.m. *n* represents the number of
979 biologically independent mice.
980
981
982 **Extended data Fig. 9: Assessment of interestial pressure, immunosurveillance and**
983 **apoptosis in CTCs at different timepoints of the circadian rhythm.**
984 **a,** Representative immunofluorescence images of Taz and Yap in CTCs collected at ZT4 and
985 ZT16 from NSG-LM2 and NSG-CDX-BR16 mice. Plots showing the distribution of Taz and
986 Yap intensity in CTCs shown in the same panel (*n*=3). Scale bar = 10 µm. **b,** Plot showing the
987 expression distribution of TEAD genes in CTCs from NSG-CDX-BR16 mice. The fold change
988 (FC, in $\log_2$ scale) and adjusted *P* value from the global differential expression analysis are
989 shown for each gene. **c,** Gating strategy to determine the frequency of the indicated cell
990 populations in panels "d" and "e". The percentage values refer to the parental population
991 considered in each panel. **d,** Plot showing the frequency of white blood cells (WBCs) from
992 peripheral blood (PB) isolated during the rest (*n*=8) or active phase (*n*=10) from BALB/c-4T1
993 mice. **e,** Plot showing the frequency of tumor-infiltrated WBCs isolated during the rest (*n*=8)
994 or active phase (*n*=10) from BALB/c-4T1 mice. **f,** Representative immunofluorescence images
995 of cleaved caspase-3 in CTCs collected at ZT4 and ZT16 from the NSG-LM2 and NSG-CDX-
996 BR16 mice. Plots showing the distribution of cleaved caspase-3 intensity in CTCs shown in
997 the same panel (*n*=3). Scale bar = 10 µm. For panels "a" and "f", center lines in the box
998 represent the median; box limits represent first and third quartile; extremes of the whisker lines
999 represent the minimum and maximum observed values. ns: non statistically significant by two-
1000 sided Mann-Whitney test. For panels "d" and "e", data are presented as mean ± s.e.m.; ns: non
1001 statistically significant by unpaired two sided *t*-test. For all panels, *n* represents the number of
1002 biologically independent mice.
1003
1004

Extended data Fig. 10: Expression of receptors activated by circadian rhythm regulated ligands.

a, Density plots showing the distribution of the average expression (log_2 counts per million) of genes encoding for receptors of circadian-regulated hormones, growth factors or molecules in CTCs from NSG-CDX-BR16 mice, NSG-LM2 mice and patients with breast cancer. Genes for the glucocorticoid receptor, androgen receptor and insulin receptor are labeled in the X-axis. **b,** Time kinetic plot showing the pharmacokinetic profile of dexamethasone-treated mice (n=2). **c,** Plots showing the size of the primary tumors dissected from dexamethasone-treated or control NSG-LM2 mice (n=4). **d,** Plots showing the size of the primary tumors dissected from testosterone-treated (n=5) or control NSG-LM2 mice (n=4). **e,** Representative bioluminescence images of lungs from untreated or testosterone-treated NSG-LM2 mice (*left*). Plot showing normalized bioluminescence signal obtained from lungs of testosterone-treated or control NSG-LM2 mice (n=3; P=0.0005). **f,** Plot showing plasma concentration of testosterone in control and testosterone-treated mice (n=3; P=0.0237). **g,** Plots showing the primary tumors dissected from control or insulin-treated mice at ZT4 and ZT16 (n=8, except insulin-treated mice at ZT16 where n=6.). **h,** Plot showing plasma concentration of insulin in control and insulin treated mice (n=5; P=0.0321). For all panels, data are presented as mean ± s.e.m.; For panels “e”, “f” and “h”, * $P < 0.05$, *** $P < 0.001$ by unpaired two sided *t*-test. For all panels, *n* represents the number of biologically independent mice.

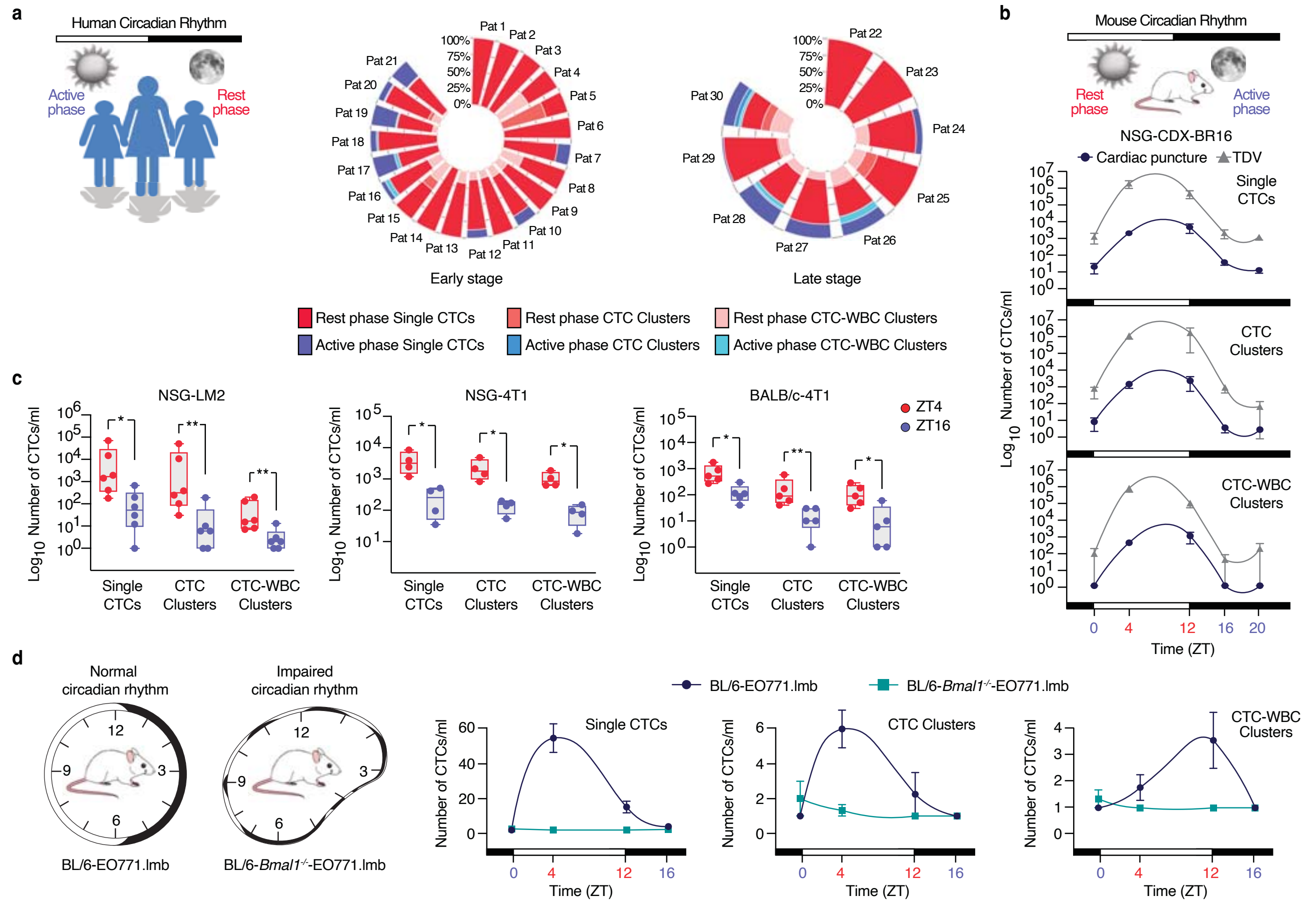

a
Human Circadian Rhythm
Active phase
Rest phase
Early stage
Late stage
Rest phase Single CTCs
Rest phase CTC Clusters
Rest phase CTC-WBC Clusters
Active phase Single CTCs
Active phase CTC Clusters
Active phase CTC-WBC Clusters
b
Mouse Circadian Rhythm
Rest phase
Active phase
NSG-CDX-BR16
Cardiac puncture
TDV
Single CTCs
CTC Clusters
CTC-WBC Clusters
Log10 Number of CTCs/ml
Time (ZT)
c
NSG-LM2
NSG-4T1
BALB/c-4T1
ZT4
ZT16
Log10 Number of CTCs/ml
Single CTCs
CTC Clusters
CTC-WBC Clusters
d
Normal circadian rhythm
Impaired circadian rhythm
BL/6-EO771.lmb
BL/6-Bmal1-/--EO771.lmb
Single CTCs
CTC Clusters
CTC-WBC Clusters
Number of CTCs/ml
Time (ZT)

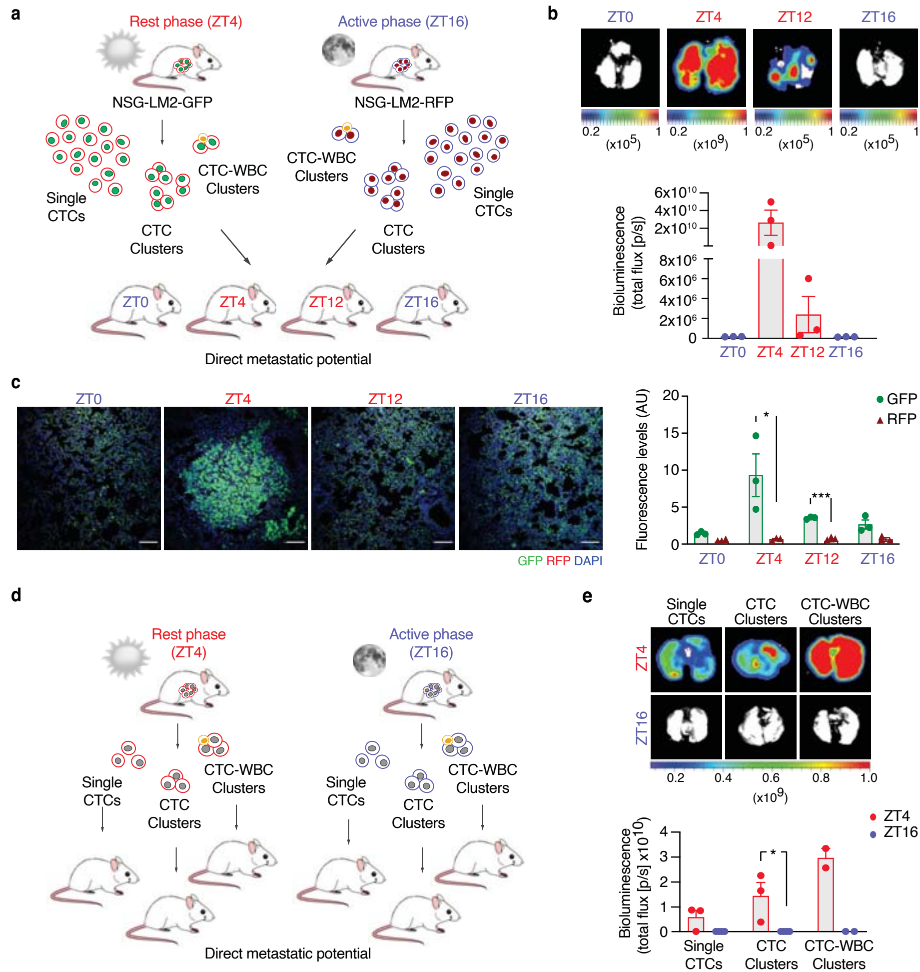
a
Rest phase (ZT4)
Active phase (ZT16)
NSG-LM2-GFP
NSG-LM2-RFP
Single CTCs
CTC Clusters
CTC-WBC Clusters
ZT0
ZT4
ZT12
ZT16
Direct metastatic potential
b
Bioluminescence (total flux [p/s])
c
GFP RFP DAPI
Fluorescence levels (AU)
GFP
RFP
d
Rest phase (ZT4)
Active phase (ZT16)
Single CTCs
CTC Clusters
CTC-WBC Clusters
Direct metastatic potential
e
ZT4
ZT16
Bioluminescence (total flux [p/s] x10^10)

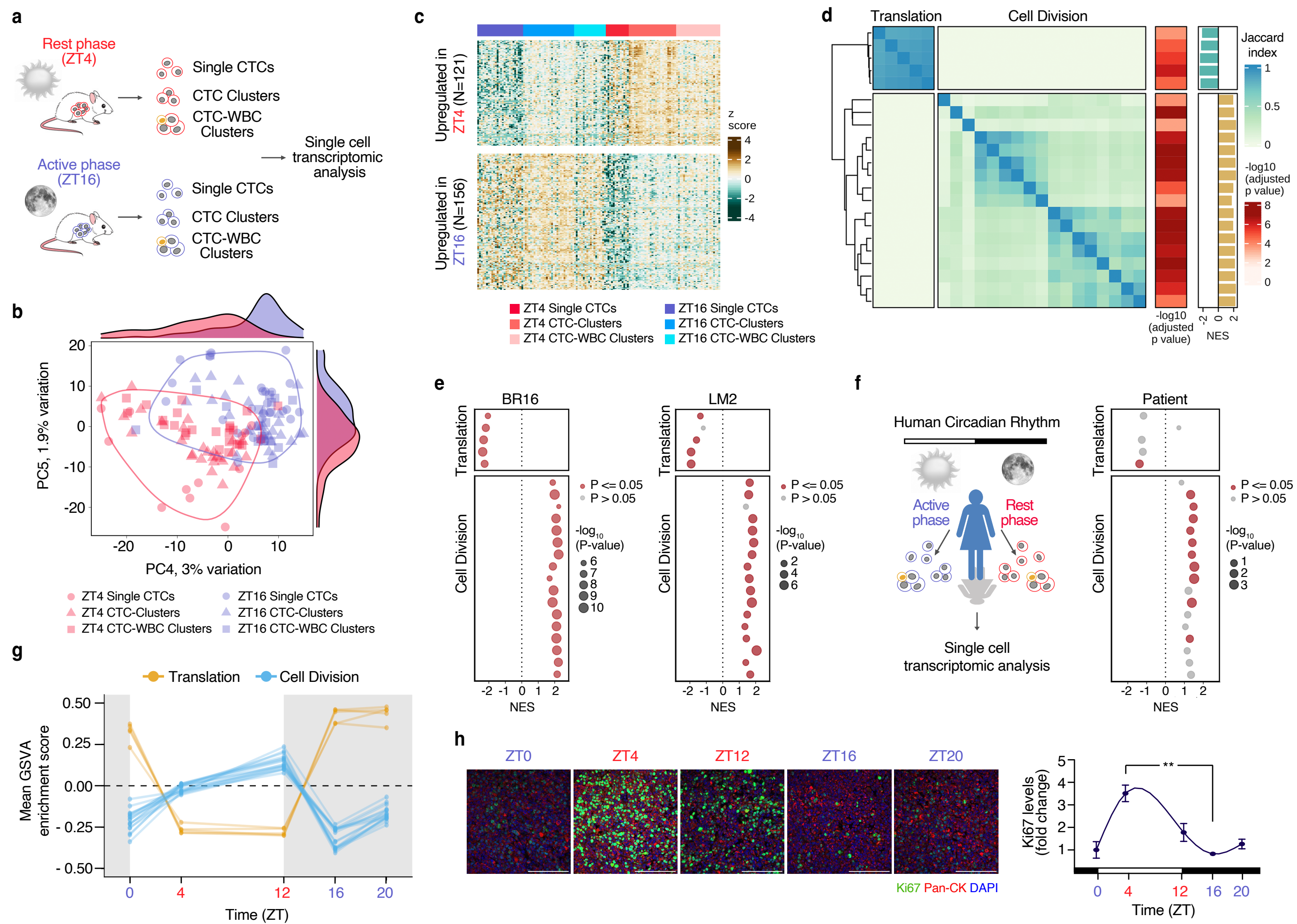

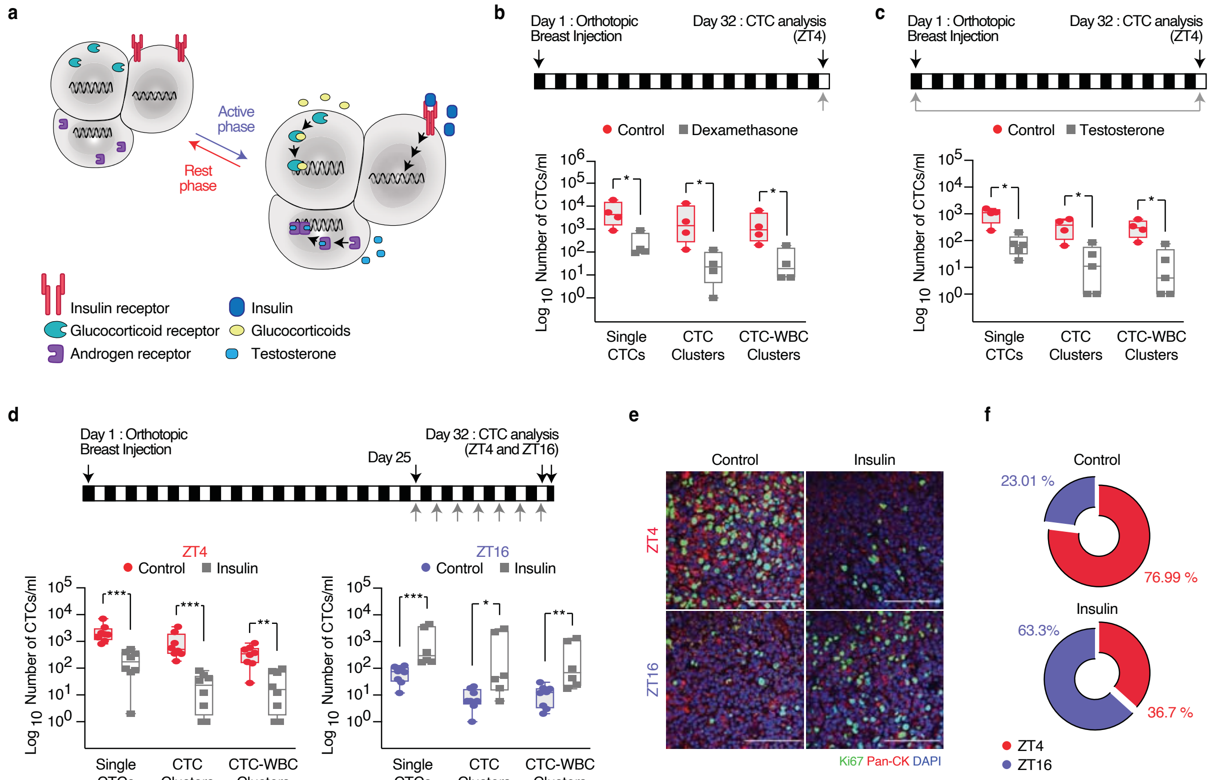

a
Active phase
Rest phase
Insulin receptor
Insulin
Glucocorticoid receptor
Glucocorticoids
Androgen receptor
Testosterone
b
Day 1 : Orthotopic Breast Injection
Day 32 : CTC analysis (ZT4)
Control
Dexamethasone
Log 10 Number of CTCs/ml
Single CTCs
CTC Clusters
CTC-WBC Clusters
c
Day 1 : Orthotopic Breast Injection
Day 32 : CTC analysis (ZT4)
Control
Testosterone
d
Day 1 : Orthotopic Breast Injection
Day 25
Day 32 : CTC analysis (ZT4 and ZT16)
ZT4
ZT16
Control
Insulin
e
Control
Insulin
ZT4
ZT16
Ki67 Pan-CK DAPI
f
Control
23.01 %
76.99 %
Insulin
63.3%
36.7 %
ZT4
ZT16